

# Asymptotic behaviour of galactic small-scale dynamos at modest magnetic Prandtl number

FREDERICK A. GENT,<sup>1,2,3</sup> MORDECAI-MARK MAC LOW,<sup>4</sup> MAARIT J. KORPI-LAGG,<sup>2,1</sup> TOUKO PURO,<sup>2</sup>  
AND MATTHIAS RHEINHARDT<sup>2</sup>

<sup>1</sup>*Nordita, KTH Royal Institute of Technology and Stockholm University, Hannes Alfvéns väg 12, Stockholm, SE-106 91 Stockholm, Sweden*

<sup>2</sup>*HPCLab, Department of Computer Science, Aalto University, P.O. Box 15400, FI-00076 Espoo, Finland*

<sup>3</sup>*School of Mathematics, Statistics and Physics, Newcastle University, NE1 7RU, UK*

<sup>4</sup>*Department of Astrophysics, American Museum of Natural History, New York, NY 10024, USA*

(Received February 17, 2026; Revised February 17, 2026; Accepted)

Submitted to ApJL

## ABSTRACT

Magnetic fields are critical at many scales to galactic dynamics and structure, including multiphase pressure balance, dust processing, and star formation. Dynamo action determines their dynamical structure and strength. Simulations of combined large- and small-scale dynamos have successfully developed mean fields with strength and topology consistent with observations but with turbulent fields much weaker than observed, while simulations of small-scale dynamos with parameters relevant to the interstellar medium yield turbulent fields an order of magnitude below the values observed or expected theoretically. We use the PENCIL CODE accelerated on GPUs with ASTAROTH to perform high-resolution simulations of a supernova-driven galactic dynamo including heating and cooling in a periodic domain. Our models show that the strength of the turbulent field produced by the small-scale dynamo approaches an asymptote at only modest magnetic Prandtl numbers. This allows us to use these models to suggest the essential characteristics of this constituent of the magnetic field for inclusion in global galactic models. The asymptotic limit occurs already at magnetic Prandtl number of only a few hundred, many orders of magnitude below physical values in the interstellar medium and consistent with previous findings for isothermal compressible flows.

*Keywords:* dynamo — magnetohydrodynamics (MHD) — ISM: supernova remnants — ISM: magnetic fields — turbulence

## 1. INTRODUCTION

We report on the results of unprecedentedly high-resolution simulations of supernova (SN)-driven turbulence in the interstellar medium

Corresponding author: Frederick A. Gent  
Email: [frederick.gent@su.se](mailto:frederick.gent@su.se), [mordecai@amnh.org](mailto:mordecai@amnh.org),  
[maarit.korpi-lagg@aalto.fi](mailto:maarit.korpi-lagg@aalto.fi), [touko.puro@aalto.fi](mailto:touko.puro@aalto.fi),  
[matthias.rheinhardt@aalto.fi](mailto:matthias.rheinhardt@aalto.fi)

(ISM) using the GPU-accelerated PENCIL CODE on the exascale resources of the LUMI supercomputer<sup>1</sup>. We reach higher magnetic Reynolds numbers than previously possible in the modelling of the *small-scale dynamo* (SSD) in the ISM. These results improve our understanding of how the turbulent magnetic field may be included more generally in simulations of galaxy formation and evolution.

Modelling the growth of galactic magnetic fields requires resolving the large separation between driving and turbulent diffusion scales. Simulations of large-scale dynamos (LSDs) have yielded solutions with large-scale fields matching the topology and field strength of those observed but with a turbulent constituents an order of magnitude weaker (Gressel 2008; Gent 2012; Gent et al. 2024). In contrast, observations determine the turbulent field constituent to be as much as ten times stronger than the mean field (Beck 2015; Beck & Berkhuisen 2025). At the low resolutions required to have time and resources to evolve the mean field, these simulations have low magnetic Reynolds numbers, which inhibits the SSD and weakens the turbulent constituent (Gressel 2008; Gent 2012). Full galaxy simulations have even lower Reynolds numbers, especially in the low-density, high sound speed regions where dynamo action is most important (Gent et al. 2023). These typically yield merely a turbulent constituent due to insufficient integration time for the mean-field dynamo to grow (Rieder & Teyssier 2016, 2017a,b; Tevlin et al. 2025).

Gent et al. (2021) and Gent et al. (2023) find that the magnetic energy at saturation of the SSD appears to approach an asymptote for magnetic Prandtl numbers  $\text{Pm} > 10$ , though the magnetic Reynolds number is the determining parameter for the strength of the field. However, the grid resolution of those simulations

**Table 1.** Models

Model	$\delta x$ [pc]	Pm	$\nu_6, \chi_6, \eta_6$ [kpc <sup>5</sup> km s <sup>-1</sup> ]	$R_{\min}$ [pc]
N128	2	[ 1,∞ ]	3 (-14)	7.0
N256	1	[ 1,∞ ]	1 (-15)	5.0
N512	1/2	[ 1,∞ ]	4 (-17)	4.5
P512	1/2	[ 1,20 ]	4 (-17)	4.5
P1024	1/4	[ 1,100 ]	2 (-18)	3.8
P2048	1/8	[ 10,500 ]	8 (-20)	3.4

NOTE—Models to benchmark dependence of  $\eta_{\text{crit}}$  on resolution are indicated by N and for testing sensitivity to Pm by P, with the number of grid points on a side given. Viscosity  $\nu = 10^{-3}$  kpc km s<sup>-1</sup> with the range of  $\text{Pm} = \nu/\eta$  given in square brackets. Sixth order hyperdiffusion coefficients are  $\nu_6 = \chi_6 = \eta_6$ .  $R_{\min}$  is the minimum radial scale  $R_{\text{SN}}$  of the SN energy injection profile. Parenthesized values give powers of ten.

was restricted to  $\delta x \in [0.5, 4]$  pc. We, therefore, extend the resolution study to the range  $\delta x \in [0.0625, 0.5]$  pc. With any numerical model there is a contribution to the diffusivity from the numerical scheme, which affects the effective Reynolds numbers and is difficult to disentangle from the explicit diffusive parameters in the model. Kriel et al. (2022, 2025) examine a method independent of explicit diffusion to determine the effective diffusivity applying from all sources to a numerical simulation. Here, however, we simply identify the explicit Lagrangian magnetic diffusivity  $\eta_{\text{crit}}$  above which the solution varies from that with purely numerical diffusion.

## 2. MODEL DESIGN

Our model domain is a periodic cubic domain of size  $h = 256$  pc on each side containing monatomic gas with mean number density  $1 \text{ cm}^{-3}$ . SNe explode intermittently at a Poisson rate  $\dot{\sigma} = 0.75\dot{\sigma}_{\text{SN}}$  at uniform random locations, where the solar neighbourhood rate

<sup>1</sup> <https://www.lumi.csc.fi/public/>

$\dot{\sigma}_{\text{Sn}} \simeq 17 \text{ kpc}^{-2} \text{ Myr}^{-1}$  (van den Bergh & Tammann 1991; Mannucci et al. 2005). The volume SN rate is determined using a galactic thickness, which we choose to be the side  $h$  of our periodic box. The periodic domain excludes pressure release by galactic winds or fountains, so we choose an SN rate lower than the solar neighborhood value to avoid thermal runaway (Kim & Ostriker 2015) and maintain a multiphase ISM for the duration of the simulations.

Our models are summarised in Table 1. Those denoted by N apply the kinematic phase of the SSD for benchmarking the magnetic diffusivity  $\eta_{\text{crit}}$  that can be resolved at each resolution (Sect. 3). Those denoted by P evolve the SSD for  $\eta > \eta_{\text{crit}}$  until saturation of the dynamo is established (Sect. 4). As a common initial condition for the set of P models, a snapshot from model N512 during its kinematic phase is used. For models with higher resolution, it is remeshed employing cubic interpolation.

To run our models, we use the PENCIL CODE<sup>2</sup> (Pencil Code Collaboration et al. 2021) coupled with the ASTAROTH<sup>3</sup> library (Pekkilä 2019; Väisälä et al. 2021; Pekkilä et al. 2022). This allows us to use GPUs for speedup by as much as a factor of 20 for this problem. We solve the compressible, non-ideal, non-adiabatic system of magnetohydrodynamic equations

$$\frac{D\rho}{Dt} = -\rho \nabla \cdot \mathbf{u} + \nabla \cdot \zeta_D \nabla \rho, \quad (1)$$

$$\begin{aligned} \rho \frac{D\mathbf{u}}{Dt} = & \mu_0^{-1} \nabla \times \mathbf{B} \times \mathbf{B} - \rho c_s^2 \nabla (s/c_p + \ln \rho) \\ & + \nabla \cdot (2\rho\nu\mathbf{W}) + \rho \nabla (\zeta_\nu \nabla \cdot \mathbf{u}) \\ & + \nabla \cdot (2\rho\nu_6\mathbf{W}^{(5)}) - \mathbf{u} \nabla \cdot (\zeta_D \nabla \rho), \end{aligned} \quad (2)$$

$$\frac{\partial \mathbf{A}}{\partial t} = \mathbf{u} \times \mathbf{B} + \eta \nabla^2 \mathbf{A} + \eta_6 \tilde{\nabla}^6 \mathbf{A}, \quad (3)$$

<sup>2</sup> <https://pencil-code.nordita.org/>

<sup>3</sup> <https://bitbucket.org/jpekkila/astaroth/src/master/>

$$\begin{aligned} \rho T \frac{Ds}{Dt} = & E_{\text{th}} \dot{\sigma} h^{-1} + \rho \Gamma - \rho^2 \Lambda + \eta \mu_0^{-1} |\nabla \times \mathbf{B}|^2 \\ & + 2\rho\nu |\mathbf{W}|^2 + \rho \zeta_\nu (\nabla \cdot \mathbf{u})^2 \\ & + \nabla \cdot (\zeta_\chi \rho T \nabla s) + \rho T \chi_6 \tilde{\nabla}^6 s \\ & - c_v \gamma T (\zeta_D \nabla^2 \rho + \nabla \zeta_D \cdot \nabla \rho), \end{aligned} \quad (4)$$

where  $\rho$  denotes the density of the gas,  $s$  its specific entropy,  $T$  its temperature, and  $\mathbf{u}$  its velocity, with  $c_s$  the adiabatic sound speed,  $t$  the time;  $\mathbf{A}$  is the magnetic vector potential, with magnetic field  $\mathbf{B} = \nabla \times \mathbf{A}$ . The constant  $\mu_0$  denotes the vacuum magnetic permeability and  $c_p$  and  $c_v$  the gas specific heat capacity at constant pressure and constant volume, respectively. The advective derivative

$$\frac{D}{Dt} = \frac{\partial}{\partial t} + \mathbf{u} \cdot \nabla, \quad (5)$$

the traceless rate of strain tensor  $\mathbf{W}$  has components

$$W_{ij} = \frac{1}{2} \left( \frac{\partial u_i}{\partial x_j} + \frac{\partial u_j}{\partial x_i} - \frac{2}{3} \delta_{ij} \nabla \cdot \mathbf{u} \right), \quad (6)$$

and  $|\mathbf{W}|^2 = W_{ij}^2$  is its contraction.<sup>4</sup>

To manage numerical instabilities near the Nyquist frequency, we apply a sixth order hyperdiffusivity in Eq. (2), proportional to the divergence of  $\rho \mathbf{W}^{(5)}$ , where

$$\mathbf{W}_{ij}^{(5)} = \tilde{\nabla}^4 W_{ij}, \quad (7)$$

and in Eqs. (3) and (4) proportional to  $\tilde{\nabla}^6 \mathbf{A}$  and  $\tilde{\nabla}^6 s$ , respectively with<sup>5</sup>

$$\tilde{\nabla}^4 = \frac{\partial^2}{\partial x_i^2} \frac{\partial^2}{\partial x_i^2}, \quad \tilde{\nabla}^6 = \frac{\partial^3}{\partial x_i^3} \frac{\partial^3}{\partial x_i^3}. \quad (8)$$

The corresponding coefficients  $\nu_6 = \eta_6 = \chi_6$  are listed in Table 1. Models at each resolution were tested to find the minimum of  $\nu_6$ , for which

<sup>4</sup> We adopt Einstein's summation convention throughout.

<sup>5</sup> Distinct from the biharmonic operator

$\nabla^4 = (\partial^2/\partial x_i^2)^2$ , etc.

the corresponding grid Reynolds number at the Nyquist frequency

$$\text{Re}^{(6)} = \frac{u_{\text{rms}}}{\nu_6 k_{\text{Ny}}^5}, \quad (9)$$

typically peaking shortly after each explosion, would remain below 10 (see [Haugen & Brandenburg 2004](#), which gives more detail on the use of hyperdiffusivity).

To resolve shock discontinuities, artificial diffusion with coefficients

$$\zeta_D, \zeta_\nu, \zeta_\chi = \begin{cases} 0.3 |\nabla \cdot \mathbf{u}|^{7/4} \text{ kpc km s}^{-1}, & \nabla \cdot \mathbf{u} < 0 \\ 0.015 |\nabla \cdot \mathbf{u}|^{7/4} \text{ kpc km s}^{-1}, & \nabla \cdot \mathbf{u} > 0 \end{cases}$$

is applied in Eqs. (1), (2), and (4), respectively. The terms with  $\zeta_D$  and  $\zeta_\chi$  are almost quadratic in  $\nabla \cdot \mathbf{u}$ , while the one with  $\zeta_\nu$  is almost cubic. Commonly, such a scheme has been applied only to convergent flows and with the exponent 1 instead of 7/4 (e.g., [Gent et al. 2020](#), with prefactor 1 instead of 0.3). We find it necessary to apply it also, albeit more weakly, to divergent flows to suppress numerical instability there, while the higher exponent better confines the diffusion locally to the shocks.

Expressions containing  $\zeta_D$  are also included in Eqs. (2) and (4) to correct for momentum and energy conservation. A missing factor in our earlier work of  $\gamma = c_p/c_v$  has been included in Eq. (4). [Srivastava et al. \(2025\)](#) found that this correction term prefactor in Eq. (4) significantly impacted the thickness of their modelled solar atmosphere, but it has limited effect in the unstratified turbulent ISM modelled here.

The system is driven and regulated by sources and sinks of heat in Eq. (4). SNe are applied with  $E_{\text{th}} = 10^{51}$  erg injected in spheres with a Gaussian radial thermal energy profile of scale  $R_{\text{SN}} \geq R_{\text{min}} \in [3.1875, 7]$  pc (as per  $\delta x$ , see Table 1), always chosen to be large enough to contain at least  $100 M_\odot$  of ambient gas within  $R_{\text{SN}}$ . Neither mass nor momentum are included

in the SN injection. Cooling following [Sánchez-Salcedo et al. \(2002\)](#) and [Gressel et al. \(2008\)](#) is implemented (see [Gent et al. 2013a](#), Table 1) but with  $\Lambda = 0$  for  $T < 90$  K, which produces thermally unstable ranges at high and low temperatures as expected for the ISM. Moreover, uniform far ultraviolet heating  $\Gamma(T)$  is included ([Wolfire et al. 1995](#)).

The ideal gas equation of state closes the system, assuming an adiabatic index  $\gamma = c_p/c_v = 5/3$ . Treating the ISM as a monatomic, fully ionized plasma we apply a mean molecular weight of 0.531. An important revision to our prior implementations is to replace third-order time integration, constrained primarily by Courant conditions, with a fourth-order accuracy-constrained adaptive time stepping scheme following [Kennedy et al. \(2000\)](#).

### 3. RESOLUTION OF MAGNETIC DIFFUSIVITY

We choose a viscosity  $\nu = 10^{-3}$  kpc km s<sup>-1</sup> because we have demonstrated that this value exceeds numerical viscosity at any resolution used in this study ([Gent et al. 2021, 2023](#)). By this, we mean that we can distinguish a difference in the energy spectrum from the solution without physical viscosity.

To identify asymptotic behavior of the SSD saturation level with respect to the magnetic Reynolds number  $\text{Rm} = l_f u_{\text{rms}}/\eta$  or Prandtl number  $\text{Pm} = \nu/\eta$ , we need to choose explicit magnetic diffusivities  $\eta$  in our simulations that exceed the numerical diffusivity. Hence, we test what values of  $\eta$  distinguish the solution from that with only hyperdiffusion and shock diffusion in runs during the kinematic phase of the SSD, labelled with N in Table 1. The magnetic energy spectra from these runs, compensated by the Kazantsev  $k^{3/2}$  scaling, are plotted in Figure 1. The insets zoom in near the start of the dissipation range, to allow identification of the critical diffusivity  $\eta_{\text{crit}}$  above which the deviations from the solutions for  $\eta = 0$  become sig-

**Table 2.** Critical magnetic diffusivity

Model	$\delta x$ [pc]	$\eta_{\text{crit}}$ [kpc km s <sup>-1</sup> ]	$k_{\eta_0}$ [kpc <sup>-1</sup> ]
N128	2	1 (-4)	460
N256	1	5 (-5)	875
N512	1/2	2 (-5)	1772

NOTE—Minimum magnetic diffusivity  $\eta_{\text{crit}}$  required to modify the solution at each resolution. Parenthesized values give powers of ten. The dissipation wavenumber  $k_{\eta_0}$  for the magnetic energy at  $\eta = 0$ , is obtained with Eq. (10).

nificant. These are listed in Table 2 and indicate that  $\eta_{\text{crit}} \approx 5 \times 10^{-5} (\delta x / 1 \text{ pc}) \text{ kpc km s}^{-1}$ .

This is confirmed quantitatively by estimating the wavenumber at the dissipation scale (see Section 12.1, Monin & Yaglom 2007, given  $k_\eta = 2\pi/l_\eta$ )

$$k_\eta = \left( \frac{\sum_k k^2 e_M(k)}{\sum_k e_M(k)} \right)^{1/2}. \quad (10)$$

To mitigate statistical noise, the energy spectra are aggregated over the final 24 snapshots for models N128–N512, spanning 1.2 Myr. The dissipation scales for models without explicit diffusivity  $k_{\eta_0} = k_\eta(\eta = 0)$  are listed in Table 2. In Figure 1(d),  $k_\eta$  normalized by  $k_{\eta_0}$  deviates from unity at  $\eta > \eta_{\text{crit}}$ .

## 4. RESULTS

### 4.1. Spectral scaling

Magnetic energy spectra for various Pm are displayed in Figure 2 for both N and P model sets. In Figure 2(a) with Pm = 1, the spectra for the models of set N in the kinematic phase align with the Kazantsev  $k^{3/2}$  scaling for  $k < k_f$  (Kazantsev 1968) while the peak energy extends to higher  $k$  with increasing resolution, where the forcing wavenumber  $k_f = 2\pi l_f^{-1}$  is determined by the correlation length of the turbulent velocity near the galactic midplane  $l_f \simeq 50 \text{ pc}$  (Hollins et al. 2017).

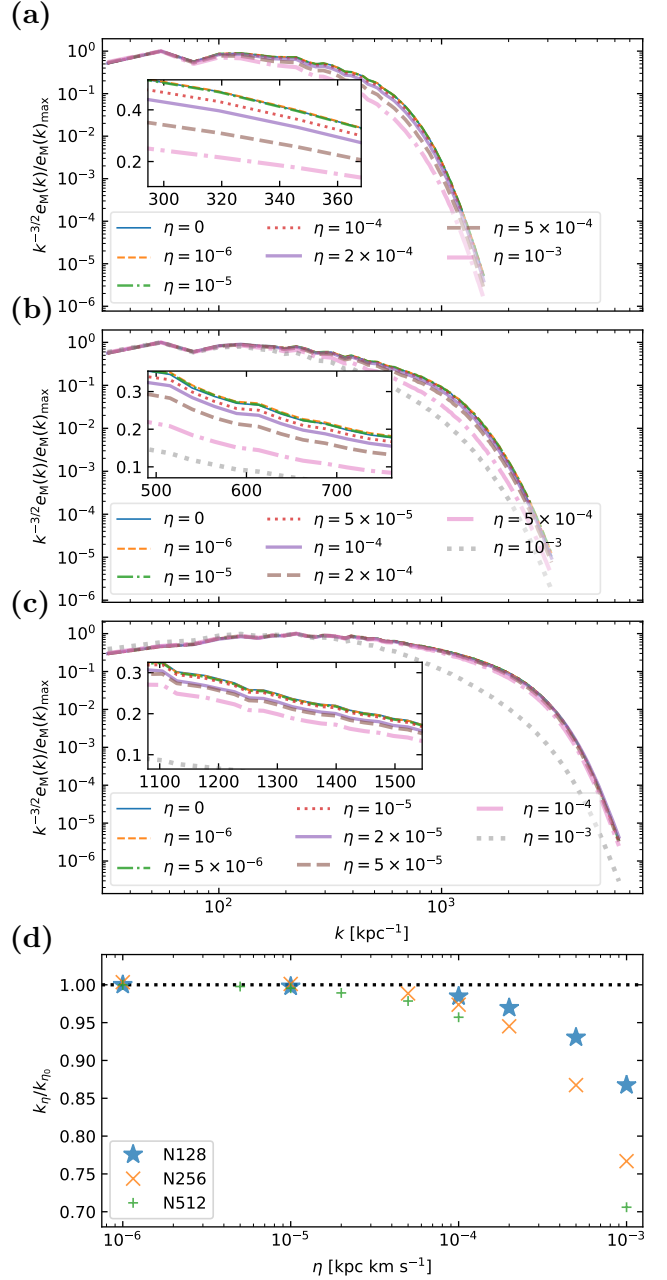


**Figure 1.** Magnetic energy spectra  $e_M(k)$  compensated by the Kazantsev scaling  $k^{3/2}$  and normalized by their compensated maximum for (a) models N128, (b) N256 and (c) N512 using different values of the magnetic diffusivity  $\eta$  in kpc km s<sup>-1</sup> as listed in the legends. Insets zoom in near the start of the inertial range to highlight deviations from the curve for  $\eta = 0$ . In panel (d), the wavenumber  $k_\eta$  at the dissipation scale, normalised by  $k_{\eta_0} = k_\eta(\eta = 0)$ , is plotted against  $\eta$ . The dissipation scale is resolved, defining  $\eta_{\text{crit}}$ , for values of  $\eta$  where  $k_\eta / k_{\eta_0} < 1$ .

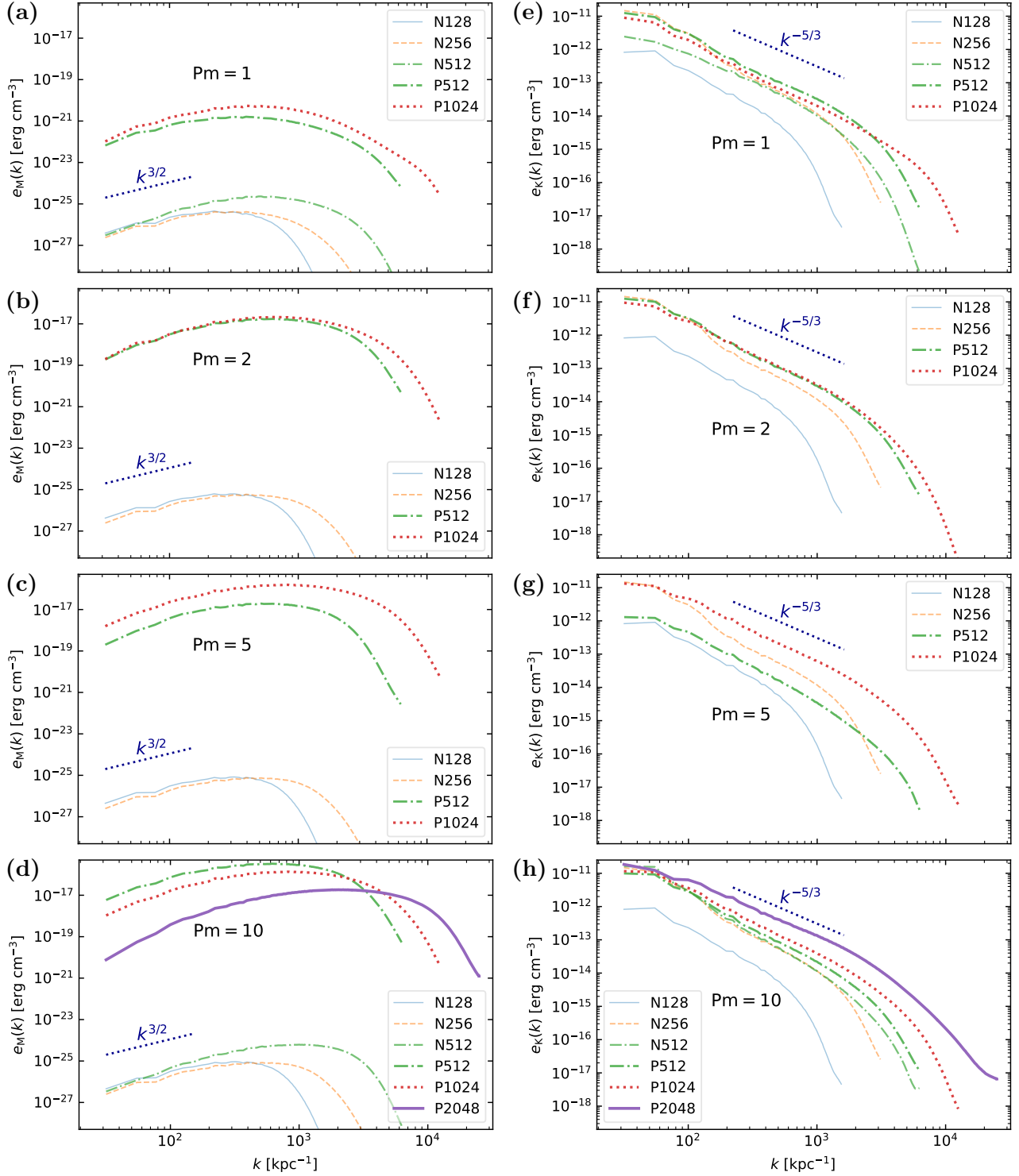


**Figure 2.** (a)–(d) Magnetic energy spectra  $e_M(k)$  at a given Pm for models listed in the legends. The  $k^{3/2}$  Kazantsev scaling is indicated lower left (dotted dark blue line). (e)–(h) Corresponding kinetic energy spectra  $e_K(k)$ . The  $k^{-5/3}$  Kolmogorov scaling is indicated in the upper centre (dotted dark blue line).

The Kazantsev scaling is also present for the models P512 and P1024, but relative to model N512, the energy peak is pushed to lower  $k$ , reflecting the apparent saturation of the SSD. This is more clearly evident in Figure 2(d) for  $\text{Pm} = 10$  when comparing the spectra for model P512 with N512 (green, dash-dotted, thick and thin, respectively). Model P512 has reached saturation and its energy peak is at significantly lower  $k \simeq 700 \text{ kpc}^{-1}$  than for model N512 at  $k \simeq 1300 \text{ kpc}^{-1}$ . Model P1024 is also approaching saturation with peak energy at even lower  $k$  than in model N512, while model P2048 is still kinematic with its peak located at even higher  $k$ . In summary, the peak energy in saturated fields converges at wavenumbers far below the Nyquist wavenumber, and Kazantsev scaling holds at lower wavenumbers.

In Figure 2(e)–(h), the kinetic energy at low resolution N128 is damped for all  $k$ , because numerical diffusion has effects beyond the dissipation range (see Gent et al. 2021, which shows that this can lead to false convergence). Above this resolution, the spectra remain well converged. The inertial range is slightly steeper than  $k^{-5/3}$ . Comparing N512 with P512 for  $\text{Pm} = 10$ , the kinetic energy is enhanced preferentially at  $k > k_\eta$  in the nonlinear SSD.

#### 4.2. Saturation

We study the saturation of models with varying  $\text{Pm}$ ,  $\text{Rm}$ , and numerical resolution, always ensuring  $\eta > \eta_{\text{crit}}$ , so the physical magnetic diffusivity determines the solution.

Figure 3 shows the evolution of the magnetic energy density  $e_M$  normalized by the time-averaged kinetic energy density  $\bar{e}_K$  for each simulation. Although the only parameter varying at fixed resolution is  $\eta$ , the models can diverge over time as the system is inherently chaotic and the time step differs in each realisation. We therefore mark SN explosions, which can be

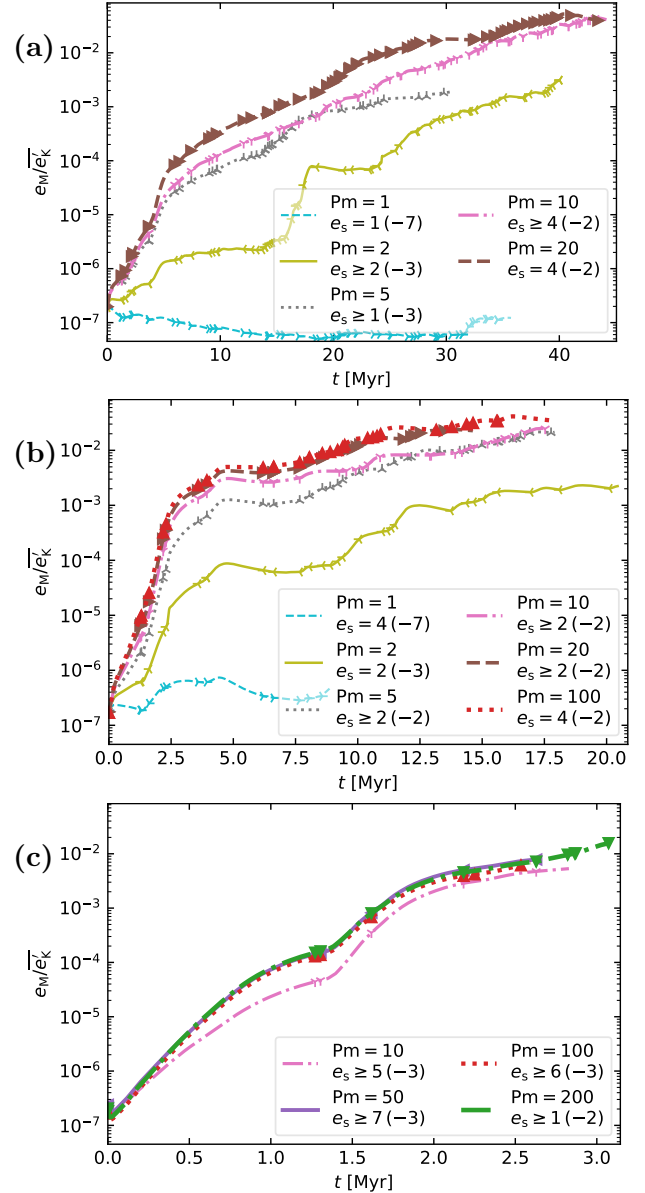


**Figure 3.** Magnetic energy  $e_M$  normalised by time-averaged turbulent kinetic energy  $\bar{e}_K$  for grid sizes (a)  $512^3$ , (b)  $1024^3$ , and (c)  $2048^3$  zones. See the legends for  $\text{Pm}$  and saturation energy  $e_s$  from an average over the final 2.5% of simulation time. Markers are shown at the time of SN explosions. Note that the time scales are dramatically smaller at higher resolution.

followed by sudden surges of magnetic energy growth.

Note that growth is substantially faster at higher resolution (Gent et al. 2021), and the

time axis covers a correspondingly shorter period of time in each panel. This indicates that the properties of the turbulence are not completely determined by the explicit values of  $\nu$  and  $\eta$  but also by the higher numerical diffusion at lower resolution.

We measure the strength of the magnetic energy after the SSD has saturated  $e_s$  relative to  $\overline{e_K}$  during the final 2.5% of run time for each simulation, and list these in the legends of Figure 3 and in Table 3. Due to our finite numerical resources, the higher resolution models in Figure 3(c) and (d) are not yet saturated, so  $e_s$  is a lower limit to the saturation level in these models. Some of the models in Figure 3(a) and (b) also do not appear to have yet fully saturated, so it would be preferable to extend those runs as well. For resolution  $N = 2048^3$  in Figure 3(c),  $e_s = 0.02$  for  $\text{Pm} = 10$  is consistent with levels obtained at the lower resolution. At higher  $\text{Rm}$ ,  $e_s$  remains below those of matching  $\text{Rm}$  runs at lower resolution. The solutions are close in Figure 3 at  $\text{Pm} = 20$  for models P512 and P1024 and the spectra are converging for these two models at  $\text{Pm} = 10$  in Figure 2(d). We find that the saturation level of the magnetic field approaches a plateau at around 5% of equipartition with the kinetic energy independent of resolution as  $\text{Pm}$  increases above 10.

The integral scale of the magnetic field, above which the field becomes weakly correlated with itself, is

$$L_B = 2\pi \frac{\sum_k k^{-1} e_M(k)}{\sum_k e_M(k)} \quad (11)$$

in the case of a solenoidal vector<sup>6</sup> (Section 12.1, Monin & Yaglom 2007). To calculate  $L_B$ , we aggregated the spectra during the final megayear of models P512–P2048 (20 snapshots for P512

and 10 snapshots otherwise). We provide the value of  $L_B$  in Table 3.

Models in the P512 family have evolved beyond the linear kinematic stage of the SSD, saturating with  $L_B \simeq 11$  pc, higher than models N512 which are still in the kinematic stage, and have  $L_B \simeq 6$  pc. Models N128 and N256 have  $L_B \simeq 21$  and 12 pc, respectively, increasing only for  $\eta \gg \eta_{\text{crit}}$  and otherwise being quite insensitive to  $\eta$ . With model P2048 also still kinematic and having  $L_B \simeq 2.5$  pc, the integral scale appears bounded by resolution during the kinematic stage of the SSD.

However, models P1024, all in the nonlinear stage of the SSD, have integral scales  $L_B > 3$  pc, which would be expected during the kinematic stage following the trends evident in models N128–N512. They may also converge on  $L_B \simeq 11$  pc, but confirmation will require the simulations to be extended. The equivalent integral scale for the velocity is consistently  $L_U \simeq 121$ –129 pc with little sensitivity to resolution, hence  $\nu = 10^{-3}$  kpc km s<sup>-1</sup> is *fully* resolved. This is somewhat smaller than  $L_\nu = 270$  pc for the turbulent flow found by Hollins et al. (2022), but that determination was in lower densities entrained by vertical winds and galactic shear.

The current results at resolutions of  $512^3$  and  $1024^3$  are strong evidence that the magnetic energy at saturation of the SSD is asymptotic at  $\text{Pm}$  or  $\text{Rm}$  levels far below those of the real ISM and within reach of numerical simulations. This is consistent with the results of Schekochihin et al. (2004) and Schober et al. (2015) for isothermal, compressible plasmas with artificial forcing, who find at  $\text{Pm} \lesssim 100$  there is already an asymptotic value of the magnetic saturation energy below 10% of equipartition with the kinetic energy.

## 5. SUMMARY AND CONCLUSIONS

Models with increasing magnetic Prandtl number  $\text{Pm}$  show that the magnetic energy density amplified by the SSD in the ISM saturates

<sup>6</sup> Gent et al. (2013b, equation [5], also Hollins et al. 2022) apply the integral scale for an isotropic *scalar* field, lower by a factor of 4, though that does not alter their conclusions.

**Table 3.** SSD saturation energy

$\eta$ [kpc km s <sup>-1</sup> ]	Pm	Rm [10 <sup>3</sup> ]			$e_s$ [ $\bar{e}_K$ ]			$L_B$ [pc]		
		at resolution [pc]			at resolution [pc]			at resolution [pc]		
		1/2	1/4	1/8	1/2	1/4	1/8	1/2	1/4	1/8
1 (-3)	1	2.8	3.0		1 (-7)*	4 (-7)*		11.3*	10.1*	
5 (-4)	2	5.8	6.3		2 (-3)	2 (-3)*		8.8	8.5*	
2 (-4)	5	9.1	20		1 (-3)	2 (-3)		11.0	6.4	
1 (-4)	10	26	29	53	4 (-2)	2 (-2)	5 (-5)	9.4	6.0	2.6
5 (-5)	20	47	54		4 (-2)*	2 (-2)		11.5*	6.2	
2 (-5)	50		263			7 (-3)				2.4
1 (-5)	100		297	555		4 (-2)*	6 (-3)		6.9*	2.3
5 (-6)	200		1165			1 (-2)				2.5

NOTE— Dependence of SSD saturation energy on  $\eta$ , Pm, and resolution. The rms velocity  $u_{\text{rms}}$  rises from 50 to 130 km s<sup>-1</sup> between  $\delta x = 1/2$  pc and 1/8 pc and varies as much as 25% for a given  $\delta x$  so Rm is not fixed for a given Pm. Saturated magnetic energy density  $e_s$  is averaged over the final 2.5% of each run, normalized by the time-averaged turbulent kinetic energy density  $\bar{e}_K$ . Applying Eq. (11), the integral scale  $L_B$  of the magnetic field is derived from the energy spectra, aggregated during the final megayear of each run. Asterisks indicate runs where the field appears saturated.

at about 5% of the turbulent kinetic energy density. This is significantly below the turbulent magnetic field energy density estimated from observations. Saturation occurs at relatively low Prandtl numbers Pm of order 10–100, while estimates of the actual Pm for the ISM are in the range  $10^{10}$ – $10^{14}$  (Brandenburg & Subramanian 2005).

In this study we have not considered the variation of the fluid Reynolds number Re, because in previous experiments Rm rather than Pm has been found to be the determining parameter for the SSD properties (Oishi & Mac Low 2011; Gent et al. 2021, 2023). However, these results were at much lower resolution, so the effect of Re should still be tested at high resolution. Even then, Re also would remain orders of magnitude below the values in the ISM. Therefore, before such results could be considered robust, we would need to find evidence as Re grows of

similar asymptotic behavior in key features of the flow as we find for the magnetic field.

It is possible that we have a false convergence in the properties of the SSD (Fryxell et al. 1991), and that at even higher Rm, new behaviour emerges. In Gent et al. (2021), a false convergence of magnetic decay for  $\delta x \geq 2$  pc at  $\eta = 10^{-3}$  kpc km s<sup>-1</sup> and  $\nu = 0$  is contradicted at  $\delta x \leq 1$  pc, for which SSD is present. However, this can be explained by the numerical diffusion dominating over the physical diffusion, whereas here we have ensured that  $\eta > \eta_{\text{crit}}$ , so any qualitative change in the behaviour of the SSD would imply that new or additional physics are acting at the smaller scales.

In these experiments, we have yet to see convergence of the growth rate in the SSD, with faster growth at higher Rm and also at higher resolution. Affecting its growth, a measure of the integral scale  $L_B$  of the magnetic field during the linear stage of the SSD appears insensi-

tive to  $R_m$ , but not to resolution in the range considered. In the nonlinear stage, we find signs of convergence in  $L_B$  across resolution and  $R_m$ . We may impute this to be a physical response to the ISM turbulence, but we need to examine how  $L_B$  responds to flows with higher  $Re$ .

From our highest resolution runs, we can verify that in the ISM we would expect a turbulent magnetic field to reach 5% of equipartition with the turbulent kinetic energy within less than 1–2 Myr. This is a timescale that is almost negligible for cosmological, galaxy cluster, or full galaxy simulations, in which it is unfeasible due to the required numerical resolution to produce by dynamo such strong magnetic fields on current computational resources. It would therefore be worth considering whether these turbulent fields might be included as an input to such simulations at the outset.

SSD production of turbulent magnetic field is absent or under-resolved in large-scale simulations. Our results suggest that it is possible to capture numerically many critical features of this process. Models of LSD that partially resolve the SSD (Gent et al. 2024) help clarify how these interact. Quantification of this process could be included in the analysis and interpretation of models in which it is underresolved or absent.

*Facilities:* The authors wish to acknowledge CSC – IT Center for Science, Finland, for computational resources. We acknowledge the

EuroHPC Joint Undertaking for awarding this project access to the EuroHPC supercomputer LUMI, hosted by CSC (Finland) and the LUMI consortium through a EuroHPC Extreme Scale Access call.

*Software:*

PENCIL CODE <https://pencil-code.nordita.org>  
 ASTAROTH <https://bitbucket.org/jpekkila/astaroth/src/master>

1 We thank the anonymous referee for construc-  
 2 tive criticism that led to improved quality and  
 3 presentation of our work. We thank C. F. Gam-  
 4 mie, C. Federrath, and J. Beattie for useful dis-  
 5 cussion of resolution diagnostics and S. Srivas-  
 6 tava & P Chatterjee for discussion regarding the  
 7 energy conservation term in Eq. (4). F.A.G.  
 8 benefited from in-depth discussions at “Towards  
 9 a Comprehensive Model of the Galactic Mag-  
 10 netic Field” at Nordita 2023 supported by Nord-  
 11 Forsk and acknowledges support of the Swedish  
 12 Research Council (Vetenskapsrådet) grant no.  
 13 2022–03767. M.J.K.-L., M.R. and T.P. ac-  
 14 knowledge support from the ERC under the  
 15 EU’s Horizon 2020 research and innovation pro-  
 16 gramme (Project UniSDyn, grant 818665). M-  
 17 M.M.L. was partly supported by US NSF grant  
 18 AST23-07950, and thanks the Inst. für The-  
 19 oretische Astrophysik der Uni. Heidelberg for  
 20 hospitality. His research was also supported in  
 21 part by grant NSF PHY-2309135 to the Kavli  
 22 Institute for Theoretical Physics (KITP).

## REFERENCES

- Beck, R. 2015, *A&A Rv*, 24, 4,  
 doi: [10.1007/s00159-015-0084-4](https://doi.org/10.1007/s00159-015-0084-4)
- Beck, R., & Berkhuijsen, E. M. 2025, *A&A*, 700,  
 A198, doi: [10.1051/0004-6361/202555048](https://doi.org/10.1051/0004-6361/202555048)
- Brandenburg, A., & Subramanian, K. 2005, *PhR*,  
 417, 1, doi: [10.1016/j.physrep.2005.06.005](https://doi.org/10.1016/j.physrep.2005.06.005)
- Fryxell, B., Mueller, E., & Arnett, D. 1991, *ApJ*,  
 367, 619, doi: [10.1086/169657](https://doi.org/10.1086/169657)
- Gent, F. A. 2012, PhD thesis, Newcastle  
 University School of Mathematics and Statistics
- Gent, F. A., Mac Low, M.-M., Käpylä, M. J.,  
 Sarson, G. R., & Hollins, J. F. 2020,  
*Geophysical and Astrophysical Fluid Dynamics*,  
 114, 77, doi: [10.1080/03091929.2019.1634705](https://doi.org/10.1080/03091929.2019.1634705)
- Gent, F. A., Mac Low, M.-M., Käpylä, M. J., &  
 Singh, N. K. 2021, *ApJL*, 910, L15,  
 doi: [10.3847/2041-8213/abed59](https://doi.org/10.3847/2041-8213/abed59)

- Gent, F. A., Mac Low, M.-M., & Korpi-Lagg, M. J. 2024, *ApJ*, 961, 7, doi: [10.3847/1538-4357/ad0da0](https://doi.org/10.3847/1538-4357/ad0da0)
- Gent, F. A., Mac Low, M.-M., Korpi-Lagg, M. J., & Singh, N. K. 2023, *ApJ*, 943, 176, doi: [10.3847/1538-4357/acac20](https://doi.org/10.3847/1538-4357/acac20)
- Gent, F. A., Shukurov, A., Fletcher, A., Sarson, G. R., & Mantere, M. J. 2013a, *MNRAS*, 432, 1396, doi: [10.1093/mnras/stt560](https://doi.org/10.1093/mnras/stt560)
- Gent, F. A., Shukurov, A., Sarson, G. R., Fletcher, A., & Mantere, M. J. 2013b, *MNRAS*, 430, L40, doi: [10.1093/mnrasl/sls042](https://doi.org/10.1093/mnrasl/sls042)
- Gressel, O. 2008, PhD thesis, Astrophysikalisches Institut Potsdam
- Gressel, O., Ziegler, U., Elstner, D., & Rüdiger, G. 2008, *Astronomische Nachrichten*, 329, 619, doi: [10.1002/asna.200811005](https://doi.org/10.1002/asna.200811005)
- Haugen, N. E. L., & Brandenburg, A. 2004, *PhRvE*, 70, 036408, doi: [10.1103/PhysRevE.70.036408](https://doi.org/10.1103/PhysRevE.70.036408)
- Hollins, J. F., Sarson, G. R., Evirgen, C. C., et al. 2022, *Geophysical and Astrophysical Fluid Dynamics*, 116, 261, doi: [10.1080/03091929.2022.2032022](https://doi.org/10.1080/03091929.2022.2032022)
- Hollins, J. F., Sarson, G. R., Shukurov, A., Fletcher, A., & Gent, F. A. 2017, *ApJ*, 850, 4, doi: [10.3847/1538-4357/aa93e7](https://doi.org/10.3847/1538-4357/aa93e7)
- Kazantsev, A. P. 1968, *Soviet Journal of Experimental and Theoretical Physics*, 26, 1031
- Kennedy, C. A., Carpenter, M. H., & Lewis, R. M. 2000, *Applied Numerical Mathematics*, 35, 177. <https://api.semanticscholar.org/CorpusID:15438200>
- Kim, C.-G., & Ostriker, E. C. 2015, *ApJ*, 802, 99, doi: [10.1088/0004-637X/802/2/99](https://doi.org/10.1088/0004-637X/802/2/99)
- Kriel, N., Beattie, J. R., Federrath, C., Krumholz, M. R., & Hew, J. K. J. 2025, *MNRAS*, 537, 2602, doi: [10.1093/mnras/staf188](https://doi.org/10.1093/mnras/staf188)
- Kriel, N., Beattie, J. R., Seta, A., & Federrath, C. 2022, *MNRAS*, 513, 2457, doi: [10.1093/mnras/stac969](https://doi.org/10.1093/mnras/stac969)
- Mannucci, F., Della Valle, M., Panagia, N., et al. 2005, *A&A*, 433, 807, doi: [10.1051/0004-6361:20041411](https://doi.org/10.1051/0004-6361:20041411)
- Monin, A., & Yaglom, A. 2007, *Statistical Fluid Mechanics, Volume 2: Mechanics of Turbulence* (M.I.T. Press)
- Oishi, J. S., & Mac Low, M.-M. 2011, *ApJ*, 740, 18
- Pekkilä, J. 2019. <https://aaltodoc.aalto.fi/server/api/core/bitstreams/c73ad7b3-47a2-4c23-b802-7721366fb961/content>
- Pekkilä, J., Väisälä, M. S., Käpylä, M. J., Rheinhardt, M., & Lappi, O. 2022, *Parallel Computing*, 111, 102904
- Pencil Code Collaboration, Brandenburg, A., Johansen, A., et al. 2021, *The Journal of Open Source Software*, 6, 2807, doi: [10.21105/joss.02807](https://doi.org/10.21105/joss.02807)
- Rieder, M., & Teyssier, R. 2016, *MNRAS*, 457, 1722, doi: [10.1093/mnras/stv2985](https://doi.org/10.1093/mnras/stv2985)
- . 2017a, *MNRAS*, 471, 2674, doi: [10.1093/mnras/stx1670](https://doi.org/10.1093/mnras/stx1670)
- . 2017b, *MNRAS*, 472, 4368, doi: [10.1093/mnras/stx2276](https://doi.org/10.1093/mnras/stx2276)
- Sánchez-Salcedo, F. J., Vázquez-Semadeni, E., & Gazol, A. 2002, *ApJ*, 577, 768, doi: [10.1086/342223](https://doi.org/10.1086/342223)
- Schekochihin, A. A., Cowley, S. C., Taylor, S. F., Maron, J. L., & McWilliams, J. C. 2004, *ApJ*, 612, 276, doi: [10.1086/422547](https://doi.org/10.1086/422547)
- Schober, J., Schleicher, D. R. G., Federrath, C., Bovino, S., & Klessen, R. S. 2015, *PhRvE*, 92, 023010, doi: [10.1103/PhysRevE.92.023010](https://doi.org/10.1103/PhysRevE.92.023010)
- Srivastava, S., Chatterjee, P., Dey, S., & Erdélyi, R. 2025, *ApJ*, 989, 39, doi: [10.3847/1538-4357/ade9b4](https://doi.org/10.3847/1538-4357/ade9b4)
- Tevlin, L., Berlok, T., Pfrommer, C., et al. 2025, *A&A*, 701, A114, doi: [10.1051/0004-6361/202452823](https://doi.org/10.1051/0004-6361/202452823)
- van den Bergh, S., & Tammann, G. A. 1991, *ARA&A*, 29, 363, doi: [10.1146/annurev.aa.29.090191.002051](https://doi.org/10.1146/annurev.aa.29.090191.002051)
- Väisälä, M. S., Pekkilä, J., Käpylä, M. J., et al. 2021, *The Astrophysical Journal*, 907, 83, doi: [10.3847/1538-4357/abceca](https://doi.org/10.3847/1538-4357/abceca)
- Wolfire, M. G., Hollenbach, D., McKee, C. F., Tielens, A. G. G. M., & Bakes, E. L. O. 1995, *ApJ*, 443, 152, doi: [10.1086/175510](https://doi.org/10.1086/175510)